Operando and Postreaction Diffraction Imaging of the La-Sr/CaO Catalyst in the Oxidative Coupling of Methane Reaction

Dorota Matras, Simon D. M. Jacques, Stephen Poulston, Nicolas Grosjean, Cristina Estruch Bosch, Benjamin Rollins, Jonathan Wright, Marco Di Michiel, Antonios Vamvakeros, Robert J. Cernik, et al.

THE JOURNAL OF PHYSICAL CHEMISTRY C

Article

Cite This: J. Phys. Chem. C 2019, 123, 1751−1760

pubs.acs.org/JPCC

Operando and Postreaction Diffraction Imaging of the La−Sr/CaO Catalyst in the Oxidative Coupling of Methane Reaction

Dorota Matras,*[,†,‡] Simon D. M. Jacques,*[,§] Stephen Poulston,[∥] Nicolas Grosjean,[∥] Cristina Estruch Bosch,[∥] Benjamin Rollins,[∥] Jonathan Wright,[⊥] Marco Di Michiel,[⊥] Antonios Vamvakeros,[§,⊥] Robert J. Cernik,[†] and Andrew M. Beale*[,‡,§,#]

[†]School of Materials, University of Manchester, Manchester, Lancashire M13 9PL, U.K.

[‡]Research Complex at Harwell, Rutherford Appleton Laboratory, Harwell Science and Innovation Campus, Didcot, Oxon OX11 0FA, U.K.

[§]Finden Limited, Merchant House, 5 East St Helen Street, Abingdon OX14 5EG, U.K.

[∥]Johnson Matthey Technology Centre, Blount's Court Road, Sonning Common, Reading RG4 9NH, U.K.

[⊥]ESRF—The European Synchrotron, Grenoble 38000, France

[#]Department of Chemistry, University College London, 20 Gordon Street, London WC1H 0AJ, U.K.

Supporting Information

ABSTRACT: A La−Sr/CaO catalyst was studied operando during the oxidative coupling of methane (OCM) reaction using the X-ray diffraction computed tomography technique. Full-pattern Rietveld analysis was performed in order to track the evolving solid-state chemistry during the temperature ramp, OCM reaction, as well as after cooling to room temperature. We observed a uniform distribution of the catalyst main components: La_2O_3, CaO−SrO mixed oxide, and the high-temperature rhombohedral polymorph of $SrCO_3$. These were stable initially in the reaction; however, doubling the gas hourly space velocity resulted in the decomposition of $SrCO_3$ to SrO, which subsequently led to the formation of a second CaO−SrO mixed oxide. These two mixed CaO−SrO oxides differed in terms of the extent of Sr incorporation into their unit cell. By applying Vegard's law during the Rietveld refinement, it was possible to create maps showing the spatial variation of Sr occupancy in the mixed CaO−SrO oxides. The formation of the Sr-doped CaO species is expected to have an important role in this system through the enhancement of the lattice oxygen diffusion as well as increased catalyst basicity.

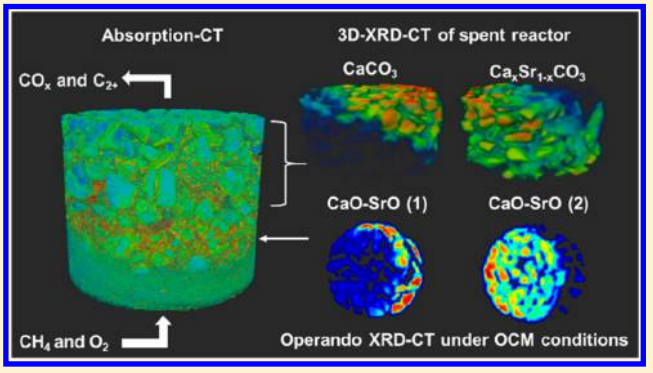

1. INTRODUCTION

The continuous depletion of crude oil, coupled with the large reserves of conventional and unconventional natural gas, especially its main component methane, renders it an increasingly important source of hydrocarbons for the chemical industry.[1] In particular, the oxidative coupling of methane (OCM), a catalytic process of methane reforming in the presence of an oxidizing agent, can potentially offer a solution for production of ethylene, one of the most important raw materials in the petrochemical industry, which is currently produced to the extent of 140−160 million tonnes per year.[2] According to a recent techno-economic assessment by Spallina et al.,[2] the OCM process can potentially become a more competitive and advantageous solution of ethylene production than the current process of ethylene production—naphtha steam cracking. However, still further development in the OCM process needs to be made, especially regarding the performance of the OCM reactor and its long-term stability. In addition, a scenario of integrating an oxygen-permeable membrane into the OCM reactor[3−5] is likely to offer a cheaper solution in terms of the air separation cost.

Multiple catalyst permutations have been tested in the OCM process, particularly those based on metal oxides, rare earth metal oxides,[6] alkaline metal oxides,[7] and transition metal oxides.[8,9] Among them, lanthanum and strontium-based catalysts have been reported to show good performance for the OCM reaction,[10] with high C_{2+} selectivity and yield (80 and 20% respectively) and no decline in its performance.[11] The high performance of La−Sr/CaO catalysts has been attributed to the strong basic sites, appropriately tailored by doping with Sr.[12,13] The significant role of catalyst basicity in the oxidative coupling reaction was pointed out by Philipp et al.[14] and Xu et

Received: September 14, 2018
Revised: November 21, 2018
Published: January 2, 2019

DOI: 10.1021/acs.jpcc.8b09018
J. Phys. Chem. C 2019, 123, 1751−1760

al.[13] A mixed alkaline earth metal oxide, for example CaO promoted by incorporation of a second alkaline earth metal oxide with higher basicity—SrO resulted in better catalyst activity and C_{2+} selectivity, when compared to a pure CaO catalyst.[13] Another important characteristic associated with Sr that plays an important role in the OCM reaction is its ability to promote and accelerate oxygen anion diffusion, necessary for active site regeneration, through the formation of a mixed oxide.[15] However, high loading of SrO (>20%) in the La−Sr/CaO catalyst may result in a decrease of its activity due to the formation of stable surface carbonates, inactive for the OCM reaction.[13] The second catalytic system, widely studied for the OCM reaction, is Na_2WO_4−Mn/SiO_2.[16,17] Although considered an excellent catalyst suitable for industrial application, its activity is inferior to the activity of the La−Sr/CaO catalyst at lower temperatures (i.e., below 800 °C),[11] especially when using a novel strategy for the catalyst design (nanostructures)[12,18,19] or monoliths with coated catalyst layer.[20,21]

The OCM process often suffers from low ethylene yields due to the formation of CO_2 and CO as a result of total and partial oxidation of methane at high temperatures (typically 800 °C). As shown in a computational fluid dynamics (CFD) analysis by Salehi et al.,[22] several different reactions occur along the length of the catalyst bed. To date, it has been possible to distinguish two main types of reaction: (1) selective oxidation, that is, oxidative coupling of methane and oxidative dehydrogenation of ethane, both yielding the production of ethylene and (2) nonselective oxidation, that is, partial and total oxidation, yielding CO_2 and CO. The nonselective reactions demand higher oxygen-to-methane ratio, thus they are more likely to occur at the beginning of the catalyst bed, where the concentration of oxygen is relatively high. After the initial high consumption of oxygen, the rate of selective oxidation reactions increases down the catalyst bed, as they demand less oxygen than nonselective reactions. The high rates of the exothermic reactions contribute to the formation of hot spots in the front of the catalyst bed.[23,24] The temperature gradient during the OCM process could be observed with our previous operando X-ray diffraction computed tomography (XRD-CT) study on La−Sr/CaO catalyst.[25] The radial temperature gradient was determined from the presence of two $SrCO_3$ polymorphs: orthorhombic, a lower temperature polymorph and rhombohedral, a higher temperature polymorph. Apart from the radial gradient, when doubling the total flow of reactive gases [the gas hourly space velocity (GHSV)], we could also observe a temporal gradient when the rhombohedral polymorph reappeared due to an increase of the catalyst bed temperature. This phenomenon was attributed to the higher ratio of nonselective reactions when applying a higher GHSV. These observations were made in the cross section collected in the middle of the catalyst bed, where it appeared that a high partial pressure of CO_2 allowed for the coexistence of both $SrCO_3$ polymorphs.[26] In order to verify the hypothesis of a temperature gradient inside the catalyst bed during the OCM process, we decided to investigate the solid-state chemistry of the La−Sr/CaO catalyst under operating conditions, but this time collecting data at the reactor inlet, where the environment surrounding the catalyst (temperature and partial pressure of CO_2) is expected to be different. Our results revealed that during the initial stage of the OCM experiment, we observed only the high temperature rhombohedral form of $SrCO_3$ and that this was uniformly distributed in the catalyst cross section. La_2O_3 and a mixed CaO−SrO phase (only one phase) were also observed. An increase in GHSV resulted in decomposition of $SrCO_3$ and formation of SrO, directly incorporated into the structure of existing mixed CaO−SrO oxide, yielding two separate mixed oxides phases, differing in the extent of Sr incorporated into their structures. The solid-state changes introduced during the OCM were maintained after cooling to room temperature, and further analysis of the spent sample showed that not only radial but also axial solid-state changes occurred during the OCM experiment.

2. EXPERIMENTAL SECTION

2.1. Catalyst Preparation. The La−Sr/CaO catalyst (10/20/70 wt %) was prepared via a modification of the nitrate and citric acid sol−gel-based method described by Olivier at al.[11] and Serres at al.[27] The sol−gel solution produced was subjected to heating, first at 120 °C for 2 h, then 300 °C for 3 h, 400 °C for 3 h and finalizing at 900 °C for 5 h, yielding the catalytic material. The temperature ramps were fixed at 1 °C min^{-1}. Finally, the prepared material was crushed and sieved, yielding fractions in the particle size of 200−400 μm.

2.2. Laboratory Fixed-Bed Measurements. A quartz reactor tube (4 mm internal diameter) was used to test 100 mg of the catalyst sample. The total flow calculated for two studied values of GHSV 36 000 and 72 000 mL·g^{-1}·h^{-1} were 60 and 120 sccm, respectively. Pure gases O_2, CH_4, and N_2 were delivered to the reactor to build 5% nitrogen dilution feed gas in three different CH_4/O_2 ratios (CH_4/O_2 2:1, 4:1, and 6:1). The catalyst was heated under an atmosphere of Ar up to 780 °C with a temperature ramp of 10 °C min^{-1}, using an electrical tube furnace. The OCM reaction was performed at atmospheric pressure and the outlet gases were analyzed by gas chromatography (Varian CP-4900 MicroGC) equipped with a thermal conductivity detector (TCD). Each condition stage of the OCM reaction lasted for 50 min.

2.3. Operando XRD-CT Measurements at ID11, ESRF. The catalyst sample (33 mg) was placed inside a quartz tube reactor (external diameter 4 mm and internal diameter 2.5 mm) to form a catalyst bed of 8 mm length, supported by glass wool. Pure gases O_2, CH_4, and He were delivered to the reactor by mass flow controllers (Brooks). The total flow calculated for the two studied values of GHSV 36 000 and 72 000 mL·g^{-1}·h^{-1} were 20 and 40 sccm, respectively. The catalyst was heated under an atmosphere of He (20 sccm) up to 780 °C with a temperature ramp of 20 °C min^{-1}, using two air gas heat blowers (Cyberstar). The OCM reaction was performed at atmospheric pressure and the outlet gases were analyzed by mass spectrometry (MS) using an Ecosys portable mass spectrometer. Two different values of GHSV (36 000 and 72 000 mL·g^{-1}·h^{-1}) as well as different ratios of CH_4/O_2 (2:1, 4:1, and 6:1) were tested for the OCM conditions. Under each OCM condition, two XRD-CT scans were performed (~25 min for one XRD-CT scan). The schematic representation of the experiment protocol can be found in the Supporting Information (Figure S1).

The XRD-CT measurements (interlaced XRD-CT[28]) were performed at ID11 beamline at the ESRF using a monochromatic beam of 55 keV with a size of 30 μm × 30 μm. Diffraction patterns were collected using a FReLoN camera, previously calibrated with a CeO_2 NIST standard. The XRD-CT scan of the catalytic reactor was performed using 180 translation steps and 160 angular steps, divided into 4 subtomo scans with an exposure time of 50 ms. Every 2D

DOI: 10.1021/acs.jpcc.8b09018
J. Phys. Chem. C 2019, 123, 1751−1760

diffraction image was converted to 1D powder diffraction pattern using the PyFAI software[29] with implemented trimmed mean filter (20%)[30] to remove the artefacts due to hot spots of crystalline materials. The reconstructed images were obtained using the filtered back projection algorithm.

2.4. 3D-XRD-CT Imaging at ID15, ESRF. 3D XRD-CT measurements were performed at ID15A beamline at the ESRF using a monochromatic beam of 89 keV with a size of 30 μm × 30 μm. Diffraction patterns were collected using a PILATUS3 X 2M CdTe (Dectris) area detector. The calibration of the detector was performed using a CeO_2 NIST standard. The continuous translation/rotation XRD-CT data collection strategy was implemented here where both tomographic axes (i.e. translation and rotation) are allowed to move simultaneously.[28] This approach led to the minimization of the dead time of the tomographic measurement. The XRD-CT scan of the catalytic reactor was performed with 100 angular steps and 100 translation steps with an exposure time of 20 ms. Consecutive XRD-CT slices were collected with the z step size of 30 μm. The total 3D-XRD-CT consisted of 36 slices which corresponded to 1.03 mm of the bed length. Every 2D diffraction image was converted to 1D powder diffraction pattern using the PyFAI software[29] with implemented trimmed mean filter (20%)[30] to remove the artefacts due to hot spots of crystalline materials. The reconstructed images were obtained using the filtered back projection algorithm.

2.5. Rietveld Refinement. Detailed information regarding phase identification and Rietveld refinement of the XRD-CT can be found in our previous work.[25] The diffraction patterns analyzed were only from tomographic voxels where the catalyst was present (regions of air, reactor vessel, and voids between particles were masked off) and the Rietveld refinement was performed on the reconstructed data.

In this study, the presented results are based on normalized scale factors (spatially-resolved data), whereas the temporal data (average diffraction pattern per line scan) during the temperature ramp are presented based on weight percent. In case of temporal changes, it is easier to operate with weight percent; however, when creating maps of the phases present, the best results are obtained using scale factors as the results are independent of the total signal from one pixel. The scale factors for each phase were normalized with respect to the maximum value obtained throughout the entire experiment, and in addition, in order to eliminate the effect of changes in the beam intensity, the obtained results were corrected in respect to the air scattering air.

In case of 3D-XRD-CT, the unknown phase was described by single peak (two reflections) and its normalized area was used for the images. All identified phases together with the crystallographic details and ICSD database code are presented in Table S1 in the Supporting Information.

3. RESULTS AND DISCUSSION

3.1. Operando XRD-CT Study. The fresh La−Sr/CaO catalyst consisted of 70% of $Ca(OH)_2$, 8% of $La(OH)_3$, and 15% of $SrCO_3$ and some small quantity of La_2O_3. These results obtained through Rietveld refinement were in good agreement with elemental analysis performed by inductively coupled plasma−MS (ICP−MS) (Table 1) for Ca and La loadings, whereas for Sr, the ICP−MS loading was almost double the quantity found through Rietveld refinement. Such difference between the estimated values through Rietveld refinement resulted from the fact that the Sr-containing phases were not fully crystalline at room temperature and thus invisible in the XRD-CT diffraction data.

Table 1. Metal Loadings on the La−Sr/CaO Catalyst Obtained through ICP−MS and Rietveld Refinement

technique	La (wt %)	Sr (wt %)	Ca (wt %)
ICP−MS	6.93	14.2	36.7
Rietveld refinement	5.12	8.9	38.9

As shown in Figure 1, during the temperature ramp in He, the following phase transformations (decompositions) were observed

$$La(OH)_3 \xrightarrow{250\ ^\circ C} LaOOH \xrightarrow{400\ ^\circ C} La_2O_3$$

$$CaCO_3 \xrightarrow{350\ ^\circ C} CaO$$

$$SrCO_3 \xrightarrow{700\ ^\circ C} SrO$$

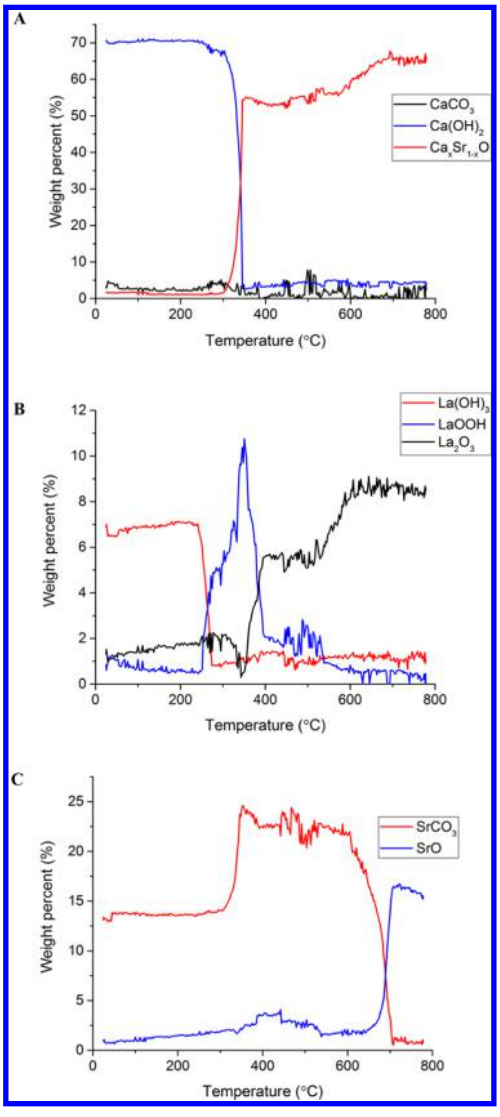

Figure 1. Total weight percent composition of the La−Sr/CaO catalyst as a function of temperature during the temperature ramp under He for panel A: crystalline phases containing Ca, panel B: crystalline phases containing La and panel C: crystalline phases containing Sr.

DOI: 10.1021/acs.jpcc.8b09018
J. Phys. Chem. C 2019, 123, 1751−1760

However, the CaO that is present in fact comprised a mixed oxide of CaO−SrO, formed mainly at the operational temperature of the OCM experiment (i.e. 780 °C). Through the combination of Vegard's law[31] and the data previously reported by Valverde and Medina,[32] Reardon and Hubbard,[33] and Beals and Cook,[34] it was possible to determine the relationship between the amount of Sr incorporated in the mixed CaO−SrO oxide and its associated lattice parameter. As the Sr^{2+} ionic radius is bigger than that of Ca^{2+} (1.18 and 1 Å respectively[35]), the substitution of 10% of Sr (in CaO) results in the increase of the lattice parameter of around 0.035 Å[33] (Figure S2). The application of this relationship in the Rietveld analysis allowed for simultaneous refinement of the occupancy factor and lattice parameter *a*, and as a result, it was possible to create a map of Sr occupancy in the mixed CaO−SrO oxides in the catalyst cross section (for cross sections collected at constant temperature).

All the events observed during the temperature ramp in this study are in agreement with previously reported studies (Table S2 in the Supporting Information) as well as in agreement with our previous study on the La−Sr/CaO catalyst.[25] The main difference with previously reported data relates to the observation of multiple $La_2O_2CO_3$ phases and the slightly lower temperature seen here for $SrCO_3$ decomposition (700 °C seen here and 750 °C reported in previous studies). It is important to note that this time, the XRD-CT data were collected at the inlet of the reactor and that this could be a factor when comparing the differences with past experiments. Because the sample was heated in an inert atmosphere (He), any CO_2 formed during the decomposition of carbonates or adsorbed on the catalyst surface would be carried with the flow of He downstream. Therefore, the probability of forming additional carbonates (such as $La_2O_2CO_3$) could have been greater for the higher parts (downstream) of the catalyst bed (in the previous study, XRD-CT data were collected in the middle of the catalyst bed) than at the inlet of the catalyst bed. Furthermore, the lower partial pressure of CO_2 at the inlet of the reactor is likely to have influenced the decomposition temperature of carbonates (mainly $SrCO_3$).[26] The increase of $SrCO_3$ at around 300 °C was most likely due to the crystallization of amorphous component present in the fresh catalyst. Additional figures presenting the evolution of solid-state chemistry during the temperature ramp and after reaching the operational temperature (i.e., 780 °C) under He can be found in the Supporting Information (Figure S3).

At the end of the temperature ramp, the composition of the crystalline components of the catalyst equaled ∼75% of CaO−SrO mixed oxide, 10% La_2O_3, and 15% SrO. The spatial distribution of phases present in room temperature and at 780 °C in He is shown in Figure 2. The Rietveld refinement fits and the estimated quantitative results are presented in the Supporting Information (Figures S4 and S5).

As it can be seen from Figure 2, the catalyst particles slightly moved after the introduction of He inside the reactor as the two panels contain different particles. From these images, we conclude that the phases present at high temperature (780 °C) were uniformly distributed inside the catalyst bed. In addition, the substitution of Sr in the mixed CaO−SrO (1) oxide was rather uniform and varied between 0.15 and 0.2.

Figure 3 shows the spatial distribution of the crystalline phases present in the catalyst during the first stage of the OCM reaction (GHSV of 36 000 $mL{\cdot}g^{-1}{\cdot}h^{-1}$). From Figure 3, we observe that the La_2O_3 phase was present in its pure form, and

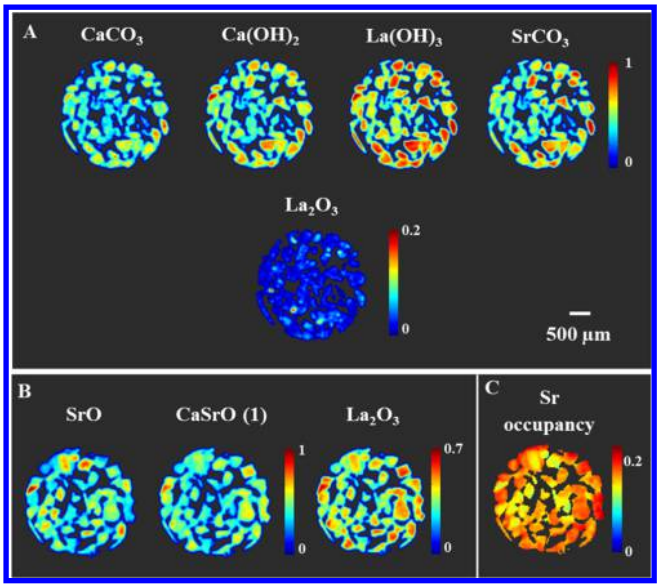

Figure 2. Spatial distribution of the La−Sr/CaO catalyst components at panel A: room temperature and panel B: at 780 °C in He. In the case of La_2O_3, the image was scaled to [0 0.2] for room temperature and [0 0.7] for 780 °C data for better visibility/contrast. Panel C: The spatial distribution occupancy of Sr in mixed CaO−SrO (1) oxide.

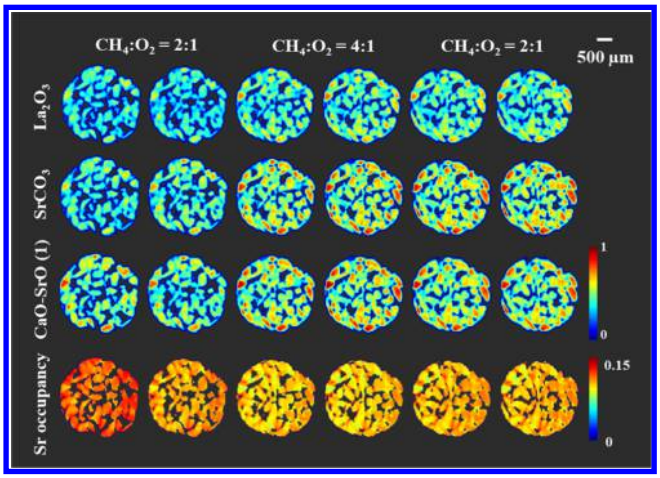

Figure 3. Spatial distribution of various crystalline catalyst components present during the OCM reaction (GHSV of 36 000 $mL{\cdot}g^{-1}{\cdot}h^{-1}$) and Sr occupancy in the mixed CaO−SrO (1) oxide. For each tested CH_4/O_2 ratio, two successive XRD-CT images were collected.

during the first stage of the OCM reaction, its quantity remained stable for conditions of the CH_4/O_2 ratio equal to 2:1. A slight increase was observed for conditions of CH_4/O_2 4:1.

After introduction of the reaction mixture, the SrO (present at the end of temperature ramp under He flow) reacted with produced CO_2 (due to the combustion reaction) and led to the formation of the rhombohedral high temperature $SrCO_3$ polymorph (see Table S1 for crystallographic information). This polymorph was observed in our previous study[25] under the OCM reaction conditions. The formation of the carbonate from the pure oxide was instantaneous, as no stabilization period after gas introduction was used. The quantity of $SrCO_3$ was shown to gradually increase during the first period of the OCM reaction. The mixed CaO−SrO (1) oxide was seen to

DOI: 10.1021/acs.jpcc.8b09018
J. Phys. Chem. C 2019, 123, 1751−1760

follow a similar trend to the La_2O_3 phase; it did not react with the products of combustion and its quantity remained constant for conditions of CH_4/O_2 2:1 but also increased during the period of CH_4/O_2 4:1. This could be attributed to a thermal effect (catalyst particle sintering), as the quantity of all phases increased during the first stage of the OCM reaction. The quantity of Sr incorporated in the mixed CaO−SrO (1) oxide started to decrease during conditions of CH_4/O_2 2:1, which could explain the slight increase in the quantity of $SrCO_3$. During the first stage of OCM, Sr occupancy decreased from 0.17 to around 0.12.

In Figure 4, the results from the second stage of the OCM reaction—GHSV of 72 000 mL·g^{-1}·h^{-1} are presented. In addition, the map after the dashed line presents the results of last XRD-CT measurements collected at GHSV of 36 000 mL·g^{-1}·h^{-1} and CH_4/O_2 4:1 (the control measurement). After doubling the GHSV, we observed the appearance of an additional phase; a second CaO−SrO. In the diffraction pattern, this was observed as a doublet of peaks characteristic for a cubic cell (see Figures S5−S7 in the Supporting Information). For Rietveld analysis, the presence of the two mixed CaO−SrO oxides was modeled as two separate cubic structures with two atoms of Ca and Sr sharing the same site. Their occupancies together with lattice parameters were refined using Vegard's law. The new phase [marked at CaO−SrO (2)] was found to form in a specific region of the catalyst bed. At the same time, we observed the disappearance of the rhombohedral polymorph of $SrCO_3$ and CaO−SrO (1) from the same area, meaning that Sr was incorporated in the unit cell of the mixed CaO−SrO (1) oxide, leading to the formation of this new phase. The formation of the new CaO−SrO (2) oxide is directly related to the increase of GHSV. The composition range of both mixed CaO−SrO oxides is represented by the colorbar axes values on Figure 4B. According to the spatial distribution of Sr occupancy in both mixed CaO−SrO oxides (Figure 4B), we can conclude that on average, the difference between the quantities of Sr in these two phases was around 15% and such a phenomenon was only possible to be captured because of the high spatial distribution and high quality of the collected diffraction patterns, analyzed with full profile Rietveld refinement. Also, in the case of the mixed CaO−SrO (1) oxide, we can observe that the quantity of Sr was higher in the areas where both oxides are present. During the first two XRD-CT scans, under the conditions of CH_4/O_2 2:1, the CaO−SrO (2) quantity increased and seemed to be present almost in the entire catalyst cross section. At conditions CH_4/O_2 4:1, the increase slowed down and finally at conditions CH_4/O_2 6:1, it started to decrease, covering only one-half of the cross section. During the last control scan, its quantity continued to decrease.

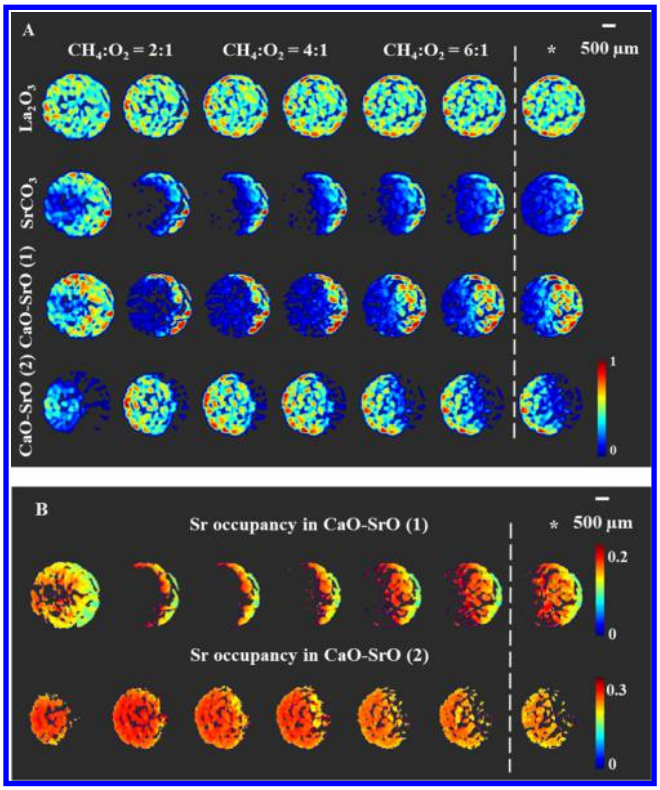

Figure 4. Panel A: Spatial distribution of components present during the OCM reaction (GHSV of 72 000 mL·g^{-1}·h^{-1}). * describes the conditions of the last measurement where the GHSV was 36 000 mL·g^{-1}·h^{-1} and the CH_4/O_2 ratio was 2:1 (note only one XRD-CT image was collected for the last measurement). Panel B: Spatial distribution of Sr occupancy in two mixed CaO−SrO oxides during the OCM reaction (GHSV of 72 000 mL·g^{-1}·h^{-1}). For each tested CH_4/O_2 ratio, two successive XRD-CT images were collected (apart from the last measurement described with *).

Regarding the $SrCO_3$ phase, its distribution in the catalyst bed (XRD-CT cross section) was anticorrelated to the CaO−SrO (2) but correlated to the CaO−SrO (1). The quantity of $SrCO_3$ decreased during the operating conditions of CH_4/O_2 ratio equal to 2:1, slowed down during the operating conditions of CH_4/O_2 equal to 4:1 and started to gradually increase when the CH_4/O_2 ratio was 6:1 and also during the control scan. Finally, the last component La_2O_3 did not seem to exhibit any changes related to these conditions. Its quantity was slightly and gradually growing.

Figure 5 presents the mean value of scale factors (normalized with respect to each other) for each phase during a particular XRD-CT scan and summarizes all the described changes.

Finally, during this experiment, we observed that the void between the catalyst particles started to disappear between the consecutive measurements (Figures S8 and S9 in the Supporting Information). The aggregation of catalyst particles was most likely caused by the gas introduction to the reactor (different CH_4/O_2 ratios and change in total flow of gas) during the experiment, and this could explain the slight increase in the scale factors for all components. In addition, the increase of the crystallite size for La_2O_3 (a stable component) was attributed to catalyst sintering caused by the high temperature in the catalyst bed (Figure S8 in the Supporting Information).

During our previous operando study of the La−Sr/CaO catalyst in the OCM reaction,[25] solid-state changes in the middle of the catalyst bed were investigated. At this point, we expected the partial pressure of CO_2 (formed as a result of combustion reactions) to be high enough in order to favor the transition between $SrCO_3$ polymorphs (orthorhombic−rhombohedral) over the decomposition of $SrCO_3$.[26] Thus, the temperature gradient inside the cross section of the catalyst bed or the increase of temperature resulting from doubling the GHSV influenced only the transition between two $SrCO_3$ polymorphs. In this study, by performing the measurement at the proximity of the reactor inlet, we indirectly show that the

DOI: 10.1021/acs.jpcc.8b09018
J. Phys. Chem. C 2019, 123, 1751−1760

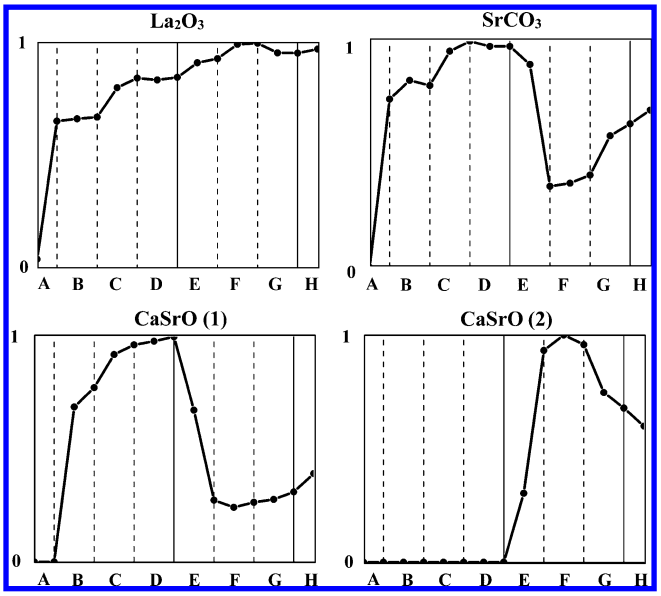

Figure 5. Plots presenting the changes in scale factors of La_2O_3, $SrCO_3$, CaO−SrO (1) and CaO−SrO (2). Region A: room temperature and high temperature measurements, region B: OCM at 2:1 CH_4/O_2 and 36 000 GHSV, region C: OCM at 4:1 CH_4/O_2 and 36 000 GHSV, region D: OCM at 2:1 CH_4/O_2 and 36 000 GHSV, region E: OCM at 2:1 CH_4/O_2 and 72 000 GHSV, region F: OCM at 4:1 CH_4/O_2 and 72 000 GHSV, region G: OCM at 6:1 CH_4/O_2 and 72 000 GHSV, and region H: OCM at 4:1 CH_4/O_2 and 36 000 GHSV.

catalyst experienced a different chemical environment (i.e., different composition of the gas phase). We observe that after the introduction of reactive gases (CH_4 and O_2) because of the high temperature and partial pressure of CO_2 the high temperature polymorph of $SrCO_3$ was formed. However, after the doubling of GHSV, this phase partially decomposed to SrO and the Sr species were incorporated inside the structure of mixed CaO−SrO oxide. According to the work performed by Iwafuchi et al.,[26] the decomposition of $SrCO_3$ was initiated by the decrease of CO_2 partial pressure, suggesting that less combustion products were formed at this position in the catalyst bed (compare to GHSV of 36 000 mL·g^{-1}·h^{-1}).

The results from the MS data collected during the OCM reaction are presented in Figure 6. It can be seen that the MS

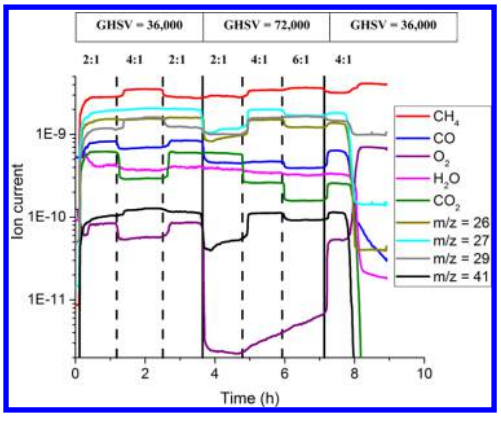

Figure 6. Results of MS during the OCM reaction for different gas compositions (CH_4/O_2 ratio) and GHSV values.

signal was directly related to the applied OCM operating conditions. Specifically, the production of CO_2 was seen to be directly related to the ratio between CH_4 and O_2; higher quantities of CH_4 resulted in a lower production of CO_2 and CO. Regarding the CH_4 conversion, this was also dependent on the imposed OCM conditions and the CH_4 conversion decreased for higher CH_4/O_2 ratios. The production of the desired molecules (m/z = 26 and m/z = 27) seemed to be similar over the first stage of the OCM reaction (for GHSV = 36 000 mL·g^{-1}·h^{-1}). Doubling of the GHSV led to a decrease of their production during the first part (CH_4/O_2 2:1) because of the lower contact time between reactants and the catalyst. For conditions CH_4/O_2 equal to 4:1 and GHSV 72 000, their production reached the previous value from conditions CH_4/O_2 4:1 and GHSV 36 000 mL·g^{-1}·h^{-1}; however, it decreased for the conditions CH_4/O_2 6:1. The MS response for m/z = 32 suggested that most of the oxygen is being consumed when a GHSV of 72 000 mL·g^{-1}·h^{-1} was used; however, at the same time, few combustion or coupling products could be observed. When comparing the last control measurement at conditions CH_4/O_2 equal to 4:1 and GHSV of 36 000 mL·g^{-1}·h^{-1}, we observed that the catalyst performance had not changed during the entire OCM study and it remained active. The obtained MS results are in agreement with the previous study[25] and both La−Sr/CaO were confirmed to be active/stable in the OCM reaction.

3.2. 3D-XRD-CT of Recovered La−Sr/CaO Catalyst.

Figure 7 presents the results from the Rietveld analysis of the

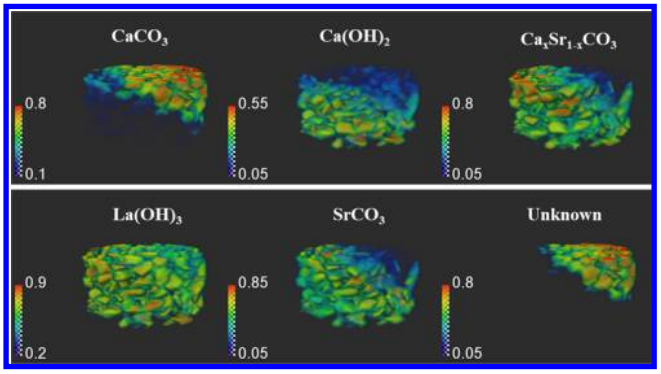

Figure 7. Volume rendering of scaled factors obtained through Rietveld refinement performed on the spent catalyst sample (recovered from operando experiment). Volumes present the normalized scale factors (in this volume) looking from the reactor inlet to the reactor outlet.

3D-XRD-CT data from the spent La−Sr/CaO catalyst bed. The sample volume probed during the 3D-XRD-CT scan did not exactly correspond to the same sample volume analyzed during the operando OCM measurement (the estimated difference between these two regions was 600 μm); however, it was close enough to provide us an estimate composition of the catalyst along the bed during the operando measurements. The probed volume represents 1.03 mm of the bed length (36 XRD-CT slices with 30 μm step). In addition, the z profile measurements were performed on this sample, covering the entire catalyst bed with the z step size of 100 μm (Figure S10). Two regions: operando XRD-CT experiments and 3D-XRD-CT measurements are marked in Figure S11.

To specify, the important information here is related to the chemical gradients both radially and axially along the length of

DOI: 10.1021/acs.jpcc.8b09018
J. Phys. Chem. C 2019, 123, 1751−1760

the reactor; this information could only be provided by a 3D-XRD-CT measurement. As it can be observed, the final components of the La−Sr/CaO catalyst (i.e. simple oxides and carbonates), after cooling to room temperature and exposure to ambient conditions, reacted with the CO_2 and H_2O present in the air, forming multiple carbonates and hydroxides. The La_2O_3 transformed into the $La(OH)_3$ and for both, their distribution inside the catalyst bed—radial and axial was uniform. Regarding the rest of the phases, we can distinguish two groups, based on their spatial distribution: (1) $Ca(OH)_2$, $SrCO_3$ and $Ca_xSr_{1-x}CO_3$ (with orthorhombic lattice cell) and (2) $CaCO_3$ and an unknown phase (described by two reflections, see Figure S12). The unknown phase was described here with two reflections (with a similar spatial distribution) and by looking at the position of these two reflections (or *d* spacing) and the chemistry of the spent catalyst sample, we suggest that this phase is based on Ca and Sr carbonates with the symmetry similar to pure $CaCO_3$.

The $SrCO_3$ and $Ca_xSr_{1-x}CO_3$ presented an anticorrelated distribution to the two other carbonates: $CaCO_3$ and the possible Ca−Sr mixed carbonate. Such segregation in spatial distribution of the identified phases may be a result of induced changes during the operando measurements, formation of mixed CaO−SrO oxides with different quantity of Sr incorporated in their structures. These solid-state changes in La−Sr/CaO induced during the OCM experiment were sustained after cooling the sample of the catalyst to room temperature, and by investigating the chemistry of the recovered catalyst sample, we can speculate about the changes occurring during the OCM reaction. As shown by 3D-XRD-CT measurements, these changes had both axial and radial characters.

3.3. Laboratory Fixed-Bed OCM Reaction. The results from laboratory OCM measurements are presented in Figure 8. As it can be observed, the results from both the operando and the laboratory fixed-bed reactor experiments were in good agreement. Methane conversion depends on the applied OCM conditions; it decreased for higher CH_4/O_2 ratios. Similar trend could be observed for the CO_2 and CO selectivity, it decreased with increased CH_4/O_2 ratios. Regarding the selectivity for C_2H_4 and C_2H_6, the trend here was opposite and higher selectivity could be obtained for higher CH_4/O_2 ratios.

The change in GHSV (from 36 000 to 72 000 $mL{\cdot}g^{-1}{\cdot}h^{-1}$) resulted in the higher conversion of CH_4, yielding mainly CO, which is a result of the partial oxidation of the methane reaction. In addition, as the partial oxidation of methane reaction is a relatively more exothermic process than the selective oxidation type reaction, the increase in catalyst bed temperature was expected. From the solid-state perspective, the change in GHSV was coincident with the partial decomposition of $SrCO_3$ and formation of SrO directly incorporated into the structure of mixed CaO−SrO, yielding two separate mixed oxide phases. This was direct evidence that the doubling of GHSV resulted in lower partial pressure of CO_2 (as the partial pressure of CO increased) and increase of temperature in the catalyst bed.

At the same time, during this stage (GHSV 72 000 $mL{\cdot}g^{-1}{\cdot}h^{-1}$ and CH_4/O_2 2:1), a slight drop in the selectivity for C_2H_4 and C_2H_6 was observed, due to the lower contact time between catalyst and reactive gases. The obtained results from the laboratory testing and the MS results from the operando experiment showed that the La−Sr/CaO catalyst was active and the catalytic performance was stable for the whole duration of the OCM experiment.

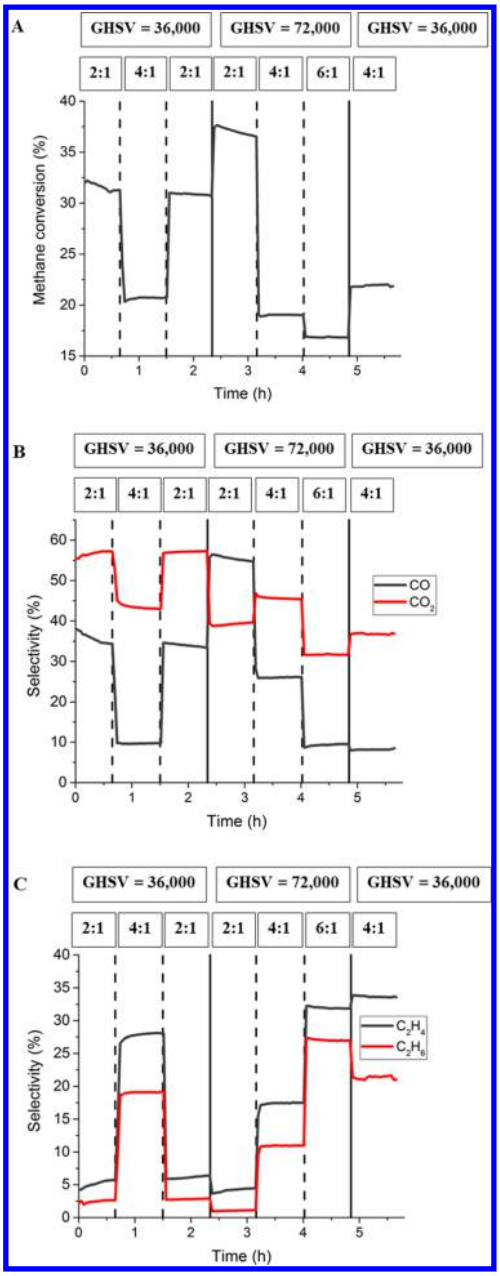

Figure 8. Panel A: Methane conversion, panel B: selectivity for CO_2 and CO, and panel C: selectivity for C_2H_4 and C_2H_6 during the OCM reaction under different conditions (CH_4/O_2 and GHSV).

4. SUMMARY AND CONCLUSIONS

In this work, we presented the results from an operando OCM experiment with a La−Sr/CaO catalyst using the XRD-CT technique in order to track the evolving solid-state chemistry under various operating conditions. Observations made during the temperature ramp—decomposition of carbonates and hydroxides of La, Ca, and Sr are in close agreement with our previous study (decomposition and its temperature) and the minor differences were attributed to the position of the bed samples (i.e. closer to the reactor inlet in this study, middle of the bed in our previous work). The results presented in this work serve to prove that the solid-state changes related to SrO

DOI: 10.1021/acs.jpcc.8b09018
J. Phys. Chem. C 2019, 123, 1751−1760

and $SrCO_3$ in the La−Sr/CaO catalyst during the OCM reaction are related to changes in the catalyst environment (partial pressure of CO_2 and temperature) and do not depend on the imposed reaction conditions (CH_4/O_2 ratio) or time on stream (i.e. not a time effect). As it is typical for catalytic systems aimed for selective methane oxidation reactions, multiple reactions occur at different parts of the catalyst bed.[22] Thus, by performing the measurement at the bottom of the catalyst bed (reactor inlet), we expected to observe different chemical evolution of the catalyst compared to our previous study (i.e., because of the catalyst being exposed to different chemical environments and temperatures). We identified the presence of a pure rhombohedral $SrCO_3$ (the high temperature form) and when the GHSV was doubled, we observed the partial decomposition of $SrCO_3$ and incorporation of the obtained Sr in the mixed oxide CaO−SrO structure. Specifically, the phase distribution maps obtained from XRD-CT showed us that this new mixed oxide started forming preferentially from one side of the catalyst bed and grew toward the other one. By using the equilibrium curves for decomposition of $SrCO_3$,[26] we could conclude that this was due to a local decrease in partial pressure of CO_2, as the catalyst was most likely experiencing radially a nonuniform composition of gas (as we observed from the XRD-CT cross section). In order to understand the reasons behind this phenomenon, more detailed studies need to be performed in the future, which could include X-ray absorption tomography imaging measurements combined with modeling and CFD.[36,37] The investigation of such catalysts as La−Sr/CaO, being sensitive to environment (partial pressure of CO_2 and temperature) under operating conditions with 3D-XRD-CT and full profile Rietveld analysis could be used to complete or verify the existing kinetic models of OCM reaction, providing an additional insight into the radial composition of the gas phase and temperature.

From a crystallographic point of view, the phenomenon of Sr incorporation into the CaO−SrO unit cell was observed as the formation of an extra peak (with the same symmetry) shifted toward lower two theta values (higher lattice parameter). Although this substitution is not significant (the estimated difference between the lattice parameters was only 0.05 Å), it was possible to observe this from the combination of the spatially resolved diffraction signals obtained with the XRD-CT technique and the full pattern Rietveld analysis of these signals. By using data previously reported in literature and Vegard's law, we refined the occupancy factor for elements (Sr and Ca) in mixed oxides, thus estimating the composition of the mixed CaO−SrO oxides. In addition, during the OCM reaction, the catalyst particles sintered because of highly exothermic reactions (combustion, partial oxidation). This was observed from the change in the crystallite size of the La_2O_3 phase (which was shown to be the most chemically stable catalyst component during the operando XRD-CT experiment).

The La−Sr/CaO catalyst showed stable catalytic performance during the OCM reaction, although multiple solid-state changes occurred during the experiment in the support material (mixed CaO−SrO oxides and catalyst particles sintering). The collected MS data and the results from the laboratory fixed-bed reactor are directly correlated to the applied OCM conditions, which was also observed in our previous study. As previously reported,[15] the beneficial role of the Sr in the regeneration of catalyst active sites comes through the enhanced oxygen diffusion and higher basicity of catalyst through the formation of mixed CaO−SrO oxides. Their presence and evolution during the OCM reaction was directly observed in this study through XRD-CT and Rietveld refinement. As observed in this study, by locking the Sr into the CaO structure, it is possible to form a phase (mixed CaO−SrO oxide) insensitive to CO_2 and thus avoid the formation of inactive $SrCO_3$.

The combination of operando XRD-CT measurements under OCM reaction conditions as well an ex situ 3D-XRD-CT of a La−Sr/CaO catalytic reactor revealed that there are significant physico-chemical heterogeneities both radially and axially, introduced during the OCM reaction and sustained when cooling to room temperature. By performing XRD-CT measurements at different parts of the catalyst bed or ideally with 5D tomographic measurements,[38] we can gain a deeper understanding of the evolving solid-state chemistry. However, the ultimate goal providing the full insight and understanding into the working catalytic reactor is the combination of spatially resolved characterization techniques,[39−41] with qualitative and/or quantitative spatially resolved gas phase analysis.[42,43]

■ ASSOCIATED CONTENT

Supporting Information

The Supporting Information is available free of charge on the ACS Publications website at DOI: 10.1021/acs.jpcc.8b09018.

Experimental protocol; crystallographic details of all identified phases; relation between lattice parameter of mixed CaO−SrO and quantity of incorporated Sr into the cubic lattice cell; review of previously reported solid-state transformations; solid-state evolution during the temperature ramp and after reaching the operational temperature (i.e., 780 °C) under He; Rietveld analysis of the operando XRD-CT data; sintering of catalyst particles during the operando OCM experiment; Z profile distribution of crystalline phases in the recovered La−Sr/CaO catalyst; absorption-CT volume of recovered La−Sr/CaO catalyst bed; and XRD-CT Rietveld analysis for recovered La−Sr/CaO catalyst (PDF)

■ AUTHOR INFORMATION

Corresponding Authors

*E-mail: dorota.matras@rc-harwell.ac.uk (D.M.).
*E-mail: simon@finden.co.uk (S.D.M.J.).
*E-mail: andrew.beale@ucl.ac.uk (A.M.B.).

ORCID

Dorota Matras: 0000-0001-6102-6405

Notes

The authors declare no competing financial interest.

■ ACKNOWLEDGMENTS

This project has received funding from the European Union's Horizon 2020 research and innovation programme under grant agreement no. 679933 (MEMERE project). A.M.B. acknowledges EPSRC (award EP/K007467/1) for funding. We acknowledge the European Synchrotron Radiation Facility for provision of synchrotron radiation facilities. We acknowledge the Advanced Characterisation Department at the Johnson Matthey Technology Centre for the elemental analyses of the fresh catalyst.

DOI: 10.1021/acs.jpcc.8b09018
J. Phys. Chem. C 2019, 123, 1751−1760

REFERENCES

(1) Olivos-Suarez, A. I.; Szécsényi, À.; Hensen, E. J. M.; Ruiz-Martinez, J.; Pidko, E. A.; Gascon, J. Strategies for the Direct Catalytic Valorization of Methane Using Heterogeneous Catalysis: Challenges and Opportunities. *ACS Catal.* **2016**, *6*, 2965−2981.

(2) Spallina, V.; Velarde, I. C.; Jimenez, J. A. M.; Godini, H. R.; Gallucci, F.; Van Sint Annaland, M. Techno-Economic Assessment of Different Routes for Olefins Production through the Oxidative Coupling of Methane (OCM): Advances in Benchmark Technologies. *Energy Convers. Manag.* **2017**, *154*, 244−261.

(3) Vamvakeros, A.; Jacques, S. D. M.; Middelkoop, V.; Di Michiel, M.; Egan, C. K.; Ismagilov, I. Z.; Vaughan, G. B. M.; Gallucci, F.; van Sint Annaland, M.; Shearing, P. R.; et al. Real Time Chemical Imaging of a Working Catalytic Membrane Reactor during Oxidative Coupling of Methane. *Chem. Commun.* **2015**, *51*, 12752−12755.

(4) Bhatia, S.; Thien, C. Y.; Mohamed, A. R. Oxidative Coupling of Methane (OCM) in a Catalytic Membrane Reactor and Comparison of Its Performance with Other Catalytic Reactors. *Chem. Eng. J.* **2009**, *148*, 525−532.

(5) Cruellas, A.; Melchiori, T.; Gallucci, F.; van Sint Annaland, M. Advanced Reactor Concepts for Oxidative Coupling of Methane. *Catal. Rev. - Sci. Eng.* **2018**, *59*, 234−294.

(6) Elkins, T. W.; Neumann, B.; Bäumer, M.; Hagelin-Weaver, H. E. Effects of Li Doping on MgO-Supported Sm2O3 and TbOx Catalysts in the Oxidative Coupling of Methane. *ACS Catal.* **2014**, *4*, 1972−1990.

(7) Olivier, L.; Haag, S.; Mirodatos, C.; van Veen, A. C. Oxidative Coupling of Methane Using Catalyst Modified Dense Perovskite Membrane Reactors. *Catal. Today* **2009**, *142*, 34−41.

(8) Zeng, Y.; Lin, Y. S. Catalytic properties of yttria doped bismuth oxide ceramics for oxidative coupling of methane. *Appl. Catal. A, Gen.* **1997**, *159*, 101−117.

(9) Kondratenko, E. V.; Schlüter, M.; Baerns, M.; Linke, D.; Holena, M. Developing Catalytic Materials for the Oxidative Coupling of Methane through Statistical Analysis of Literature Data. *Catal. Sci. Technol.* **2015**, *5*, 1668−1677.

(10) Choudhary, V. R.; Mulla, S. A. R.; Uphade, B. S. Oxidative Coupling of Methane over Alkaline Earth Oxides Deposited on Commercial Support Precoated with Rare Earth Oxides. *Fuel* **1999**, *78*, 427−437.

(11) Olivier, L.; Haag, S.; Pennemann, H.; Hofmann, C.; Mirodatos, C.; Vanveen, A. High-Temperature Parallel Screening of Catalysts for the Oxidative Coupling of Methane. *Catal. Today* **2008**, *137*, 80−89.

(12) Song, J.; Sun, Y.; Ba, R.; Huang, S.; Zhao, Y.; Zhang, J.; Sun, Y.; Zhu, Y. Monodisperse Sr-La2O3 hybrid nanofibers for oxidative coupling of methane to synthesize C2 hydrocarbons. *Nanoscale* **2015**, *7*, 2260−2264.

(13) Xu, Y.; Yu, L.; Cai, C.; Huang, J.; Guo, X. A Study of the Oxidative Coupling of Methane over SrO-La2O3/CaO Catalysts by Using CO2 as a Probe. *Catal. Letters* **1995**, *35*, 215−231.

(14) Philipp, R.; Omata, K.; Aoki, A.; Fujimoto, K. On the Active Site of MgO/CaO Mixed Oxide for Oxidative Coupling of Methane. *J. Catal.* **1992**, *134*, 422−433.

(15) Kechagiopoulos, P. N.; Olivier, L.; Daniel, C.; van Veen, A. C.; Thybaut, J. W.; Marin, G. B.; Mirodatos, C. Combining Catalyst Formulation and Microkinetic Methodologies in the Detailed Understanding and Optimization of Methane Oxidative Coupling. In *Small-Scale Gas to Liquid Fuel Synthesis*; CRC Press: Boca Raton, 2015; pp 227−261.

(16) Arndt, S.; Otremba, T.; Simon, U.; Yildiz, M.; Schubert, H.; Schomäcker, R. Mn-Na2WO4/SiO2 as catalyst for the oxidative coupling of methane. What is really known? *Appl. Catal. A Gen.* **2012**, *425-426*, 53−61.

(17) Gambo, Y.; Jalil, A. A.; Triwahyono, S.; Abdulrasheed, A. A. Recent Advances and Future Prospect in Catalysts for Oxidative Coupling of Methane to Ethylene: A Review. *J. Ind. Eng. Chem.* **2018**, *59*, 218−229.

(18) Hou, Y.-H.; Han, W.-C.; Xia, W.-S.; Wan, H.-L. Structure Sensitivity of La2O2CO3 Catalysts in the Oxidative Coupling of Methane. *ACS Catal.* **2015**, *5*, 1663−1674.

(19) Huang, P.; Zhao, Y.; Zhang, J.; Zhu, Y.; Sun, Y. Exploiting shape effects of La2O3 nanocatalysts for oxidative coupling of methane reaction. *Nanoscale* **2013**, *5*, 10844−10848.

(20) Sollier, B. M.; Gómez, L. E.; Boix, A. V.; Miró, E. E. Oxidative coupling of methane on cordierite monoliths coated with Sr/La2O3 catalysts. Influence of honeycomb structure and catalyst-cordierite chemical interactions on the catalytic behavior. *Appl. Catal. A Gen.* **2018**, *550*, 113−121.

(21) Sollier, B. M.; Gómez, L. E.; Boix, A. V.; Miró, E. E. Oxidative coupling of methane on Sr/La 2 O 3 catalysts: Improving the catalytic performance using cordierite monoliths and ceramic foams as structured substrates. *Appl. Catal. A Gen.* **2017**, *532*, 65−76.

(22) Salehi, M.-S.; Askarishahi, M.; Godini, H. R.; Görke, O.; Wozny, G. Sustainable Process Design for Oxidative Coupling of Methane (OCM): Comprehensive Reactor Engineering via Computational Fluid Dynamics (CFD) Analysis of OCM Packed-Bed Membrane Reactors. *Ind. Eng. Chem. Res.* **2016**, *55*, 3287−3299.

(23) Aseem, A.; Jeba, G. G.; Conato, M. T.; Rimer, J. D.; Harold, M. P. Oxidative coupling of methane over mixed metal oxide catalysts: Steady state multiplicity and catalyst durability. *Chem. Eng. J.* **2018**, *331*, 132−143.

(24) Karakaya, C.; Zhu, H.; Zohour, B.; Senkan, S.; Kee, R. J. Detailed Reaction Mechanisms for the Oxidative Coupling of Methane over La2 O3 /CeO2 Nanofiber Fabric Catalysts. *ChemCatChem* **2017**, *9*, 4538−4551.

(25) Matras, D.; Jacques, S. D. M.; Godini, H. R.; Khadivi, M.; Drnec, J.; Poulain, A.; Cernik, R. J.; Beale, A. M. Real-Time Operando Diffraction Imaging of La-Sr/CaO During the Oxidative Coupling of Methane. *J. Phys. Chem. C* **2018**, *122*, 2221−2230.

(26) Iwafuchi, K.; Watanabe, C.; Otsuka, R. On the Transition Temperatures of BaCO3 and SrCO3 as DTA Temperature Reference Materials. *Thermochim. Acta* **1983**, *64*, 381−386.

(27) Serres, T.; Dreibine, L.; Schuurman, Y. Synthesis of Enamel-Protected Catalysts for Microchannel Reactors: Application to Methane Oxidative Coupling. *Chem. Eng. J.* **2012**, *213*, 31−40.

(28) Vamvakeros, A.; Jacques, S. D. M.; Di Michiel, M.; Senecal, P.; Middelkoop, V.; Cernik, R. J.; Beale, A. M. Interlaced X-Ray Diffraction Computed Tomography. *J. Appl. Crystallogr.* **2016**, *49*, 485−496.

(29) Ashiotis, G.; Deschildre, A.; Nawaz, Z.; Wright, J. P.; Karkoulis, D.; Picca, F. E.; Kieffer, J. The fast azimuthal integration Python library:pyFAI. *J. Appl. Crystallogr.* **2015**, *48*, 510−519.

(30) Vamvakeros, A.; Jacques, S. D. M.; Di Michiel, M.; Middelkoop, V.; Egan, C. K.; Cernik, R. J.; Beale, A. M. Removing Multiple Outliers and Single-Crystal Artefacts from X-Ray Diffraction Computed Tomography Data. *J. Appl. Crystallogr.* **2015**, *48*, 1943−1955.

(31) Denton, A. R.; Ashcroft, N. W. Vegard's law. *Phys. Rev. A: At., Mol., Opt. Phys.* **1991**, *43*, 3161−3164.

(32) Valverde, J. M.; Medina, S. Crystallographic Transformation of Limestone during Calcination under CO2. *Phys. Chem. Chem. Phys.* **2015**, *17*, 21912−21926.

(33) Reardon, B. J.; Hubbard, C. R. *A Comprehensive Review of the XRD Data of the Primary and Secondary Phases Present in BSCCO Superconductor System: Part 1, Ca-Sr-Cu Oxides*; Tennessee, 1992.

(34) Beals, R. J.; Cook, R. L. Directional Dilatation of Crystal Lattices at Elevated Temperatures. *Peratu Res. J. Am. Ceram. Soc.* **1957**, *40*, 279−284.

(35) Shannon, R. D. Revised effective ionic radii and systematic studies of interatomic distances in halides and chalcogenides. *Acta Crystallogr., Sect. A: Cryst. Phys., Diffr., Theor. Gen. Crystallogr.* **1976**, *32*, 751−767.

(36) Yang, L.; Liu, F.; Song, Z.; Liu, K.; Saito, K. 3D Numerical Study of Multiphase Counter-Current Flow within a Packed Bed for Post Combustion Carbon Dioxide Capture. *Energies* **2018**, *11*, 1441.

DOI: 10.1021/acs.jpcc.8b09018
J. Phys. Chem. C 2019, 123, 1751−1760

(37) Min, J.; Drake, J. B.; Heindel, T. J.; Fox, R. O. Experimental Validation of CFD Simulations of a Lab-Scale Fluidized-Bed Reactor with and Without Side-Gas Injection. *AIChE J.* **2009**, *56*, 1434−1446.
(38) Vamvakeros, A.; Jacques, S. D. M.; Di Michiel, M.; Matras, D.; Middelkoop, V.; Ismagilov, I. Z.; Matus, E. V.; Kuznetsov, V. V.; Drnec, J.; Senecal, P.; et al. 5D Tomographic Operando Diffraction Imaging of a Catalyst Bed. *Nat. Commun.* **2018**, *9*, 4751.
(39) Jacques, S. D. M.; Michiel, M. Di; Kimber, S. A. J.; Yang, X.; Cernik, R. J.; Beale, A. M.; Billinge, S. J. L. Pair Distribution Function Computed Tomography. *Nat. Commun.* **2013**, *4*, 2536.
(40) Jacques, S. D. M.; Di Michiel, M.; Beale, A. M.; Sochi, T.; O'Brien, M. G.; Espinosa-Alonso, L.; Weckhuysen, B. M.; Barnes, P. Dynamic X-Ray Diffraction Computed Tomography Reveals Real-Time Insight into Catalyst Active Phase Evolution. *Angew. Chem., Int. Ed.* **2011**, *50*, 10148−10152.
(41) Beale, A. M.; Jacques, S. D. M.; Di, M.; Mosselmans, J. F. W.; Stephen, W. T.; Senecal, P.; Vamvakeros, A.; Paterson, J.; Senecal, P.; Vamvakeros, A.; et al. X-Ray Physico-Chemical Imaging during Activation of Cobalt-Based Fischer−Tropsch Synthesis Catalysts. *Phil. Trans. R. Soc. A* **2017**, *376*, 1−14.
(42) Touitou, J.; Morgan, K.; Burch, R.; Hardacre, C.; Goguet, A. An in Situ Spatially Resolved Method to Probe Gas Phase Reactions through a Fixed Bed Catalyst. *Catal. Sci. Technol. Catal. Sci. Technol* **2012**, *2*, 1811−1813.
(43) Zohour, B.; Noon, D.; Senkan, S. New Insights into the Oxidative Coupling of Methane from Spatially Resolved Concentration and Temperature Profiles. *ChemCatChem* **2013**, *5*, 2809−2812.

DOI: 10.1021/acs.jpcc.8b09018
J. Phys. Chem. C 2019, 123, 1751−1760